Nitrogen/chlorine-doped carbon nanodisk-encapsulated hematite nanoparticles for high-performance lithium-ion storage

Yajuan Li, Tianchen Xia, Tingting Yu, Yingchun Miao, Meng Yang, Xiangyu Zhao, Liqun Ma

PII: S0925-8388(20)32409-9

DOI: https://doi.org/10.1016/j.jallcom.2020.156045

Reference: JALCOM 156045

To appear in: *Journal of Alloys and Compounds*

Received Date: 2 May 2020

Revised Date: 9 June 2020

Accepted Date: 10 June 2020

Please cite this article as: Y. Li, T. Xia, T. Yu, Y. Miao, M. Yang, X. Zhao, L. Ma, Nitrogen/chlorine-doped carbon nanodisk-encapsulated hematite nanoparticles for high-performance lithium-ion storage, *Journal of Alloys and Compounds* (2020), doi: https://doi.org/10.1016/j.jallcom.2020.156045.

Yajuan Li, Data curation; Investigation; Methodology; Writing-original draft;
Tianchen Xia, Investigation;
Tingting Yu, Investigation;
Yingchun Miao, Investigation; Resources
Meng Yang, Methodology; Investigation;
Xiangyu Zhao, Conceptualization; Methodology; Supervision; Writing-review & editing; Funding acquisition
Liqun Ma, Supervision; Project administration;

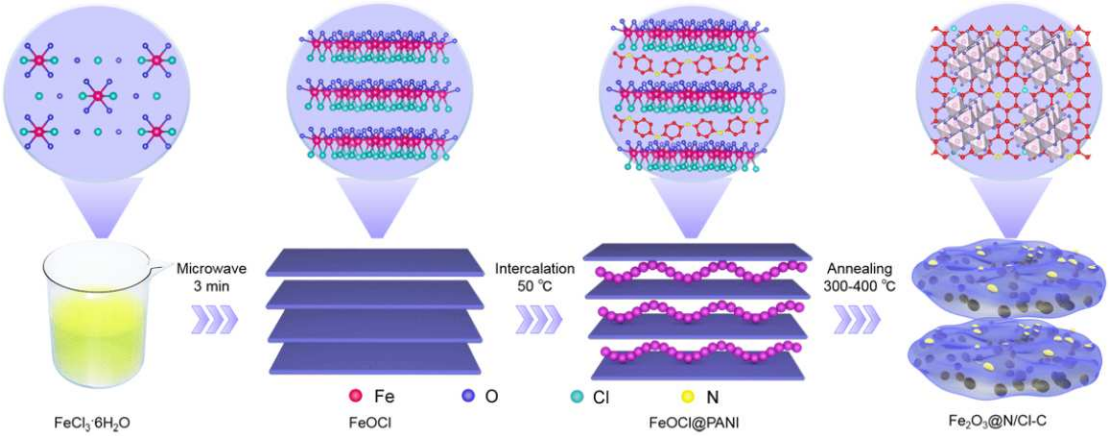

Nitrogen/chlorine-doped carbon nanodisk-encapsulated hematite nanoparticles for high-performance lithium-ion storage

Yajuan Li[a], Tianchen Xia[a], Tingting Yu[b], Yingchun Miao[c], Meng Yang[a,d], Xiangyu Zhao[a,d,*], Liqun Ma[a]

[a] *College of Materials Science and Engineering, Nanjing Tech University, Nanjing 211816, China*

[b] *Department of Chemical and Materials Engineering, Hefei University, Hefei 230601, China*

[c] *Advanced Analysis and Testing Center, Nanjing Forestry University, Nanjing 210037, China*

[d] *Jiangsu Collaborative Innovation Center for Advanced Inorganic Functional Composites, Nanjing Tech University, Nanjing 211816, China*

* Corresponding author.

Email: xiangyu.zhao@njtech.edu.cn

ABSTRACT

Iron oxide (Fe_2O_3) is an intriguing anode material of electrochemical energy storage systems such as rechargeable batteries. The rational design of its nanostructure at mild condition to cope with the issues of low reversible capacity and sluggish kinetics is required. Herein, an efficient, facile, and potentially large-scale synthesis approach using the precursor of laminated iron oxychloride@polyaniline heterostructure and mild annealing is developed, yielding unique Fe_2O_3@carbon nanocomposites with hematite nanoparticles (~ 20 nm) that embedded in nitrogen/chlorine-doped carbon nanodisk (N/Cl-C). Given the benefit of abundant active sites, good chemical contact between carbon and Fe_2O_3, and robust composite structure, the as-prepared Fe_2O_3@N/Cl-C anode material delivers competent lithium-ion storage properties, including high reversible capacity of 1010 mAh g^{-1} (based on the mass of the as-prepared nanocomposite) at 0.1 A g^{-1}, decent rate performance upon a rigorous current change, and superior cycling stability with 955 mAh g^{-1} after 180 cycles as well as a sustained Coulombic efficiency of about 99%. This structural design may provide a new avenue for achieving efficient iron oxide-based materials in chemical and electrochemical applications such as catalysis, lithium-ion batteries, and sodium-ion batteries.

Keywords: Iron oxide; nitrogen/chlorine-doped carbon; rechargeable batteries; iron oxychloride; polyaniline

1. Introduction

Versatile iron oxides such as Fe_2O_3 and Fe_3O_4 have been developed for diverse applications such as catalysis [1], biomedicine [2], chemical adsorption [3], and gas sensing [4]. Considering their high chemical stability, abundant elemental resources, nontoxicity, and high theoretical capacity, iron oxides are also regarded as intriguing anode materials for rechargeable batteries such as lithium-ion and sodium-ion batteries [5,6]. For instance, Fe_2O_3, as a naturally occurring material, shows an impressive theoretical capacity of about 1007 mAh g^{-1} that is 2.7 times larger than that of graphite. However, its application was hindered by sluggish electronic and ionic transport, large volume change upon ion storage, and severe agglomeration of active material during cycling, which led to poor cycling performance and low reversible capacity of Fe_2O_3 electrodes [7,8].

To cope with the above issues, two kinds of effective strategies, including design of nanostructures and preparation of composite materials, have been developed [7-12]. The formation of nanoscale materials could facilitate the reversible ion storage of Fe_2O_3 because of abundant active surface, the decrease in the ion diffusion length, and the alleviation of lattice strain by volume change [13-15], thereby achieving enhanced reversible capacity. The combination of nanoscale Fe_2O_3 with a second phase or a ductile and conductive matrix such as carbon material or conducting polymer could further improve its electrochemical properties [16-18]. For instance, Zhou el al. used a template-engaged redox reaction and a subsequent annealing to fabricate a ladder-like

α-Fe_2O_3 nanostructure at a high temperature of 800 °C for 5 h, which showed good structural stability against repeated lithiation [15]. Ni et al. reported that surface sulfurization of electrochemically anodized Fe_2O_3 nanotube arrays (about 1.4 μm in thickness) or a low-valent iron and nitrogen dual doping of Fe_2O_3 nanorods on carbon cloth achieved significant enhanced charge carrier transport and reaction activity, thus enabling large reversible capacity and outstanding rate capability [19,20]. Kang et al. synthesized hollow Fe_2O_3 nanospheres embedded in an amorphous carbon matrix through a multistep heating of an electrospun precursor. This unique hollow structure could accommodate the volume variation upon cycling [21]. Zhang et al. designed a Fe_2O_3@carbon material with robust yolk-shell structure, which was formed by etching the SiO_2 layer of Fe_2O_3@SiO_2@carbon and allowed the lithiation induced expansion of the Fe_2O_3 core, and thus contributed to a superior cycling stability [17,22]. The SiO_2 layer can also avoid the reduction reaction of Fe_2O_3 during the high-temperature (600 °C, 3 h) carbon coating process. Similar design concept has been used to synthesize the multishelled Fe_2O_3@SnO_2@carbon material with an active intermediate SnO_2 layer [5]. Although some achievements on the Fe_2O_3 anode materials have been obtained, the rational structural design and scalable preparation of high-performance Fe_2O_3-based materials without high processing cost and complex technologies are still highly desired.

Herein, we report a new facile, efficient, and low-cost approach using a FeOCl@polyaniline precursor with a laminated heterosturcture to synthesize a series of hematite@carbon nanocomposites, which consist of nitrogen/chlorine-doped

carbon nanodisk (N/Cl-C) and hematite nanoparticles that are uniformly embedded in the amorphous carbon nanodisk. The evolution of structure, composition, and morphology of the precursor upon annealing has been systematically investigated. The as-prepared Fe_2O_3@N/Cl-C shows good contact between the carbon matrix and Fe_2O_3, robust composite structure during lithium-ion storage, and abundant active sites, thereby achieving superior electrochemical performance with a high reversible capacity of 955 mAh g^{-1} after 180 cycles at 0.1 Ah g^{-1}. The relationship between the structure and electrochemical properties of the as-prepared Fe_2O_3@N/Cl-C materials has been elucidated.

2. Experimental

2.1 Synthesis of materials

Iron oxychloride (FeOCl) was fabricated using a microwave heating method. The $FeCl_3 \cdot 6H_2O$ (Aladdin, ACS) was loaded in a glass bottle and heated in a microwave oven (700 W) for 3 min. The obtained product of FeOCl was washed using acetone (Lingfeng, AR) to remove the residue $FeCl_3$ species and dried at 60 °C for 10 h under vacuum. The as-prepared FeOCl material (2 g) was added into the purified aniline solution (2 ml, 98%, Alfa Aesar) with constant magnetic stirring at 50 °C for 18-36 h under argon atmosphere, yielding the FeOCl@polyaniline (FeOCl@PANI) materials. Then, this precursor was heated at 200 °C for 1 h under argon atmosphere, followed by a further annealing at 300, 350, 400, 450, or 500 °C for 5 min (heating rate: 5 °C min^{-1}) to prepare the iron oxide/carbon materials. Finally, the product was washed with ethanol, and then dried overnight under vacuum at 60 °C.

2.2 Materials characterization

X-ray diffraction (XRD) data were recorded by using a Rigaku SmartLab diffractometer (Cu-Kα radiation). Elemental (vario EL III, USA) and thermal (NETZSCH 449 F3) analyses were carried out to measure the nitrogen and carbon contents in the as-prepared materials. The Fourier transform infrared spectroscopy (FTIR) spectra were collected on a Thermo Nicolet Nexus 670 Spectrometer (400 to 4000 cm^{-1} wave number range). Raman spectra were obtained from a Raman spectroscopy (Labram HR800, 532 nm laser beam). The morphology and microstructure were investigated using the field-emission scanning electron microscopy (FE-SEM, Ultra55) and transition electron microscopy (TEM, Tecnai G2 F30 S-Twin). X-ray photoelectron spectroscopy (XPS, AXIS UltraDLD) was conducted to characterize the bonding state and elemental components.

2.3 Electrochemical measurements

The electrodes were fabricated using a common slurry coating approach. The active material, carbon black, and polyvinylidene fluoride (PVDF) binder (weight ratio, 8:1:1) were mixed in the N-methyl-2-pyrrolidone (NMP) solvent to make a slurry, which was coated on a clean and dried Cu foil and then dried overnight under vacuum at 80 °C. Electrochemical half-cells (CR2032) were assembled using the working electrode of the as-prepared electrode, the separator of Celgard 2400 film, and the lithium metal foil anode. The electrolyte was a 1 M $LiPF_6$ in ethylene carbonate (EC), dimethyl carbonate (DMC), and diethyl carbonate (DEC) (volume ratio, 1 1: 1).

The charge and discharge testing were performed using a Neware battery system in a

voltage range of 0.01-3 V versus Li^+/Li at room temperature. Cyclic voltammetry (CV) tests at a scan rate of 0.05 mV s^{-1} were conducted using a Bio-logic (VMP3) electrochemical workstation in a voltage range of 0.01-3 V versus Li^+/Li.

3. Results and Discussion

Fig. 1 shows the schematic preparation process of hematite@nitrogen/chlorine-doped carbon (Fe_2O_3@N/Cl-C) materials and XRD patterns of FeOCl, FeOCl@PANI, and Fe_2O_3@N/Cl-C materials. The high-efficiency transformation (~91%) from $FeCl_3 \cdot 6H_2O$ to FeOCl was achieved by the microwave heating for only 3 min. This approach is much convenient for producing FeOCl compared to the chemical vapor transport (CVT) at 370 ^oC for several days and the thermal decomposition at 180-250 ^oC for several hours [23,24]. Upon the aniline treatment for 18 h, the as-prepared FeOCl material showed a large interlayer expansion and the fully intercalation by polyaniline, as demonstrated by the disappearance of the (010) main diffraction peak at 11.2° (7.9 Å) and the formation of a new diffraction peak at 6.4° (13.8 Å) [25,26]. This intercalation occurred because of the interaction between the aniline monomer (−NH−) and the chlorine in the interlayers of FeOCl by the formation of the hydrogen bond (H−Cl). The polyaniline layer was subsequently formed in the interlayers through the oxidative polymerization by the Fe^{3+} (Fe−Cl) of FeOCl, thereby forming a laminated heterostructure consisting of FeOCl and polyaniline monolayers [25,27].

The elemental analysis (Supplementary EA) manifested that the as-prepared laminated FeOCl@PANI (18 h) possessed a polyaniline component of about 15.1 wt% (20.5 at%) on the basis of the detected carbon and nitrogen contents. The prolonged

aniline treatment to 36 h kept the phase structure of FeOCl@PANI, and led to a slight increase in the polyaniline content to 16 wt% (22 at%), yielding a formula of $PANI_{0.22}FeOCl$. This content is much higher than 17 at% of the previously reported polyaniline-intercalated FeOCl [28], in which the FeOCl material prepared by the CVT method showed a large particle size and required a very long time of six days for the full polyaniline intercalation. This further indicates the facile and highly efficient preparation of FeOCl by the microwave heating. Moreover, a higher polyaniline content is beneficial to the formation of a more integrated polyaniline layer in the interlayers of FeOCl. Upon a further treatment to 48 h, the layered structure was destroyed because of the excess decrement of the Fe^{3+} (Fe-Cl) by the polymerization reaction; instead, the ultrafine α-Fe_2O_3 phase (PDF card No. 72-469) was formed (Fig. S1) [28], indicating the formation of the Fe_2O_3@PANI material, although a small fraction of the FeOCl@PANI material still existed.

The as-prepared laminated FeOCl@PANI material (36 h) was annealed under argon atmosphere to fabricate the iron oxide/carbon materials at different temperatures, which were selected according to the results of the thermal analysis (Fig. S2a). A continuous weight loss occurred during the heating process. The initial weight loss in the thermogravimetric (TG) curve at about 150 °C was dominated by the release of the adsorbed water, followed by the loss of anionic chloride species from PANI at about 200 °C [29,30]. The following weight loss is due to the decomposition of FeOCl and polyaniline. Fig. 1c shows the XRD patterns of the annealed samples. Upon the annealing at 300 °C, the α-Fe_2O_3 with a small grain size of about 19 nm (based on the

Scherrer's formula) was formed, indicating the decomposition of FeOCl component in the laminated FeOCl@PANI material. The byproduct of iron chloride species was removed during the washing process using organic solvent. Meanwhile, the crosslinking of the PANI chains and the reorganization of carbon and nitrogen bonds occurred [31]. The decomposition of FeOCl was completed at about 350 °C according to the formation of an endothermic reaction at this temperature and a plateau region in the range of 350-400 °C in the differential scanning calorimetry (DSC) curve (Fig. S2). The samples treated at higher temperatures of 350 and 400 °C also showed the reflections of α-Fe_2O_3 materials with increased grain sizes of about 22 and 29 nm, respectively. The EA results demonstrated that the carbon and nitrogen contents in the samples decreased from 15.7 to 15.2 wt% and increased from 2.5 to 2.8 wt%, respectively, upon an annealing temperature increase from 350 to 400 °C. The chlorine content in the as-prepared materials will be analyzed later. Note that the (110) and (104) peak ratio increased after the 400 °C annealing, which may be due to the formation of few Fe_3O_4 from the reduction reaction of Fe_2O_3 by the amorphous carbon that was produced from the decomposition of PANI. This reaction was confirmed by a prolonged annealing for 15 min at the same temperature that the distinct diffraction peaks of Fe_3O_4 were formed in the XRD pattern (Fig. S3). The further increase in the annealing temperature to 450 °C also led to the formation of a mixture of Fe_2O_3 and Fe_3O_4 (PDF card No. 72-2303) (Fig. S3), indicating the obvious reaction between Fe_2O_3 and carbon. The pure Fe_3O_4 was formed at 500 °C.

Fig. 2 shows the electron microscopy results of the as-prepared materials. The

distinct expanded interlayers of FeOCl by the intercalation of PANI were observed from the High-resolution TEM (HRTEM) images (Fig. 2a-d). This confirms the peak shift in the XRD patterns. A distinct lattice distortion was also observed after this intercalation. The SEM image (Fig. S4) showed that the polyaniline was also coated on the surface of the as-prepared FeOCl nanoflakes, indicating the excellent combination between FeOCl and polyaniline from interlayer to surface layer. The following annealing resulted in the formation of a distinct and uniform cookies-like morphology of nanodisks embedded with ultrafine nanoparticles (Fig. 1a and Fig. 2g,h), which showed an increase in the particle size as the annealing temperature increased. These nanoparticles showing a particle/grain size of ~20 nm are determined to α-Fe_2O_3 phase by TEM, HRTEM, and the corresponding fast Fourier transform (FFT) pattern (Fig. 2e,f). This is consistent with XRD result for the annealed materials. The annealing at 400 °C led to the severe agglomeration of these nanoparticles into an integrated nanoplate in the amorphous carbon nanodisk matrix (Fig. 2i). This nanodisk morphology was destroyed upon the annealing at a higher temperature of 450 °C because of the reaction between α-Fe_2O_3 and the carbon matrix, which also caused the formation of Fe_3O_4 polyhedrons at 500 °C (Fig. S4). The EDS analysis for the as-prepared samples (Fig. S5) indicated that the nitrogen element was introduced into the sample by the PANI intercalation, which also led to a decrease in the chlorine content due to the polymerization of aniline. A further decrease in the chlorine content occurred by the annealing at 300 °C because of the decomposition of FeOCl, as confirmed by the decrease of the chlorine to iron atomic ratio (Cl/Fe: from 0.6 to

0.36), which tended to be stable at 350-400 °C (Cl/Fe: ~ 0.15). This also demonstrated the full decomposition of FeOCl that was observed in the DSC curve. The TG analysis (Fig. S2b) for the as-prepared Fe_2O_3/carbon nanocomposites derived at 350 and 400 °C indicated that their total carbon, nitrogen, and chlorine contents are 23.7 and 22.6 wt%, respectively. Their chlorine contents can be calculated to be 5.5 and 4.8 wt%, respectively, by considering the carbon and nitrogen contents derived from the EA results. The explicit elemental composition of the as-prepared Fe_2O_3@N/Cl-C materials are therefore obtained.

Fig. 3 shows the FTIR and Raman curves of the as-prepared materials. The FeOCl material showed a characteristic absorption band at around 500 cm^{-1} that is ascribed to the Fe-O stretching vibration [27], which was kept after the PANI intercalation that induced the formation of evident PANI signals in the range of 600-1600 cm^{-1} (Table S1). For instance, the quinonoid ring and C–C aromatic ring stretching vibrations appeared at 1569 and 1493 cm^{-1}, respectively. The AnH^+ signal at 745 and 687 cm^{-1}, the aromatic C–H in-plane bending modes between 1010 and 1170 cm^{-1}, and the C-N stretching mode at 1315 and 1250 cm^{-1} were also observed [28,31]. The following annealing led to the formation of dominant signals located at 549 and 467 cm^{-1}, which are related to the Fe-O stretching vibration in α-Fe_2O_3 [11,32]. The carbon-based signals are weak because of its low content in the as-prepared nanocomposites; however, some evident changes upon annealing can still be observed. The disappearance of the bands at about 687, 745, and 1140 cm^{-1} suggested the full deprotonation of PANI by annealing. The signals of the benzene ring at 1493 cm^{-1} and aquinonoid ring at 1569

cm^{-1} were weakened and shifted to higher positions. This may be ascribed to the crosslinking of carbon-based chains and rearrangement of carbon and nitrogen bonds. The peak of the C-N in-plane stretching modes at 1303 and 1250 cm^{-1} moved toward a lower position [31,33-35]. Furthermore, the bands at 1164 and 826 cm^{-1} may be correlated with C-Cl bonds. The band at 1164 cm^{-1} shifted toward a higher positon at a higher annealing temperature [36]. A new signal appeared at 756 cm^{-1} may be attributed to the formation of phenazine units by the bond breaking and cross-linking.

The as-prepared FeOCl material shows characteristic Raman peaks of Fe-O stretching vibrations at 334, 370, and 638 cm^{-1}. The band at 200 cm^{-1} may be related to the Fe-Cl bond [37,38]. For the as-prepared FeOCl@PANI material, the distinct signals of PANI are detected (Table S2). For instance, the C-C stretching vibrations were reflected at about 1559 and 1618 cm^{-1}. The $C\text{-}N^{+\cdot}$ (charge delocalization) vibrations were correlated to the band at about 1340 cm^{-1}. A broad region around 1190 cm^{-1} was ascribed to the C-N stretching vibrations and/or C-H bending vibration of quinonoid rings. The several weak bands between 700 and 900 cm^{-1} were attributed to deformations of aromatic rings [31,35]. The Fe-O signal was not shown in the Raman spectrum because the surface of the FeOCl@PANI material was covered by PANI (Fig. S4) [38]. When the laminated FeOCl@PANI was annealed at 300 °C, the five bands between 200 and 600 cm^{-1} appeared because of the formation of α-Fe_2O_3 [39,40]. Moreover, the characteristic Raman peaks of PANI disappeared; instead, the weak signal corresponding to carbonaceous material was observed. The evident G and D bands at 1559 (a weak shoulder at 1410 cm^{-1}) and 1295 cm^{-1} [31,41], respectively, was

shown by the annealing at 350 °C. The increased ratio of I_G/I_D implicated an enhanced ordered carbon structure. However, this ratio decreased after the annealing at 400 ^oC. This may be caused by the slight reduction reaction between carbon and α-Fe_2O_3 [39].

Fig. 4 shows the XPS spectra of the C 1s, N 1s, and Cl 2p for the FeOCl@PANI and Fe_2O_3@N/Cl-C materials. The C 1s spectrum collected from the surface of FeOCl@PANI exhibits deconvoluted peaks of C-C/C-H (284.5 eV), C-N/C=N/C-H (285.1 eV), C-N^+/C=N^+/C-Cl (286.0 eV), and C=O/C-O (288.9 eV) [42,43]. After the annealing at 350 °C, a strong signal at 284.8 eV related to carbonaceous material and a secondary peak at 286.0 eV (C-N/C-O/C-Cl) were observed (Fig. 4a) [43,45]. This indicates the formation of N/Cl-doped carbon material. In addition, the minor peak at 288.9 eV may be attributed to the C=O/C(O)O [46], which could hardly be detected for the samples annealed at 450 and 500 ^oC (Fig. S6). This bond may indicate the well chemical combination or interaction between the α-Fe_2O_3 nanoparticles and carbon nanodisk matrix; however, it was weakened by the higher temperature annealing because of the reaction between α-Fe_2O_3 and carbon to form Fe_3O_4. For the N 1s region spectra (Fig. 4b), three deconvoluted components centered at 399.5 (-NH-), 400.4 (polaron), and 401.9 eV (bipolaron) are obtained for the as-prepared FeOCl@PANI material [28]. The corresponding pyridinic nitrogen (N-6) at 399.5 eV and pyrrole or pyridone nitrogen (N-5) at 400.5 eV were produced in the as-prepared Fe_2O_3@N/Cl-C material (350 ^oC) [47]. These nitrogen species were also formed in other carbon materials prepared by pyrolyzing polymers and were beneficial to modify the polarity and electron distribution of carbon, thereby improving ion

diffusion [48]. A new peak at 401.4 eV appeared by the annealing at 400 ^{o}C, which led to the breaking of N-5 bond to form a quaternary nitrogen species (N-Q) [47]. However, upon the further increase of the annealing temperature, the content of N-6 and N-Q decreased compared to that of N-5. This may be due to that the N-6 and N-Q were consumed by the aforementioned internal reaction of the as-prepared Fe_2O_3@N/Cl-C material. Consequently, N-Q was depleted at 500 ^{o}C [49]. The Cl 2p signals did not show evident variation before and after annealing. A distinct pair of Cl 2p peaks was located at 198.5 and 200.1 eV for the as-prepared FeOCl@PANI material [50,51]. This Cl 2p signal was derived from the PANI coating because the pure FeOCl exhibited the Cl 2p signal at 198.8 and 200.4 eV [52]. Similar Cl 2p peaks were obtained in the as-prepared Fe_2O_3@N/Cl-C materials, although the PANI component has been pyrolyzed to carbon after the annealing. The chlorine doping in the carbon material was considered to be helpful to enhance the electrochemical active sites [53-55].

Fig. 5 shows the electrochemical properties of the Fe_2O_3@N/Cl-C electrodes for lithium storage. The CV profiles in the initial cycles of the Fe_2O_3@N/Cl-C-300, Fe_2O_3@N/Cl-C-350, and Fe_2O_3@N/Cl-C-400 electrodes exhibited explicit redox peaks. The irreversible cathodic reactions in the first cycle may be associated with the reduction of some oxidative groups of carbon material (above 1.5 V vs Li/Li^+) and the formation of solid-electrolyte interphase (SEI) layer (below 1.0 V vs Li/Li^+) [15], which caused capacity loss and low initial Coulombic efficiency (CE). The redox reactions in the following cycles showed good reversibility, as confirmed by the well overlapped CV curves. The high reversibility also demonstrates that the formation of

the SEI layer was completed in the first cycle, thereby contributing to a decreased electrochemical polarization and thus the emergence of distinct cathodic peak at higher potential in the following cycles. This cathodic peak is ascribed to the lithiation of Fe_2O_3 to form Fe and Li_2O by a two-step transformation reaction [22,56]. The corresponding multi-step oxidation reaction from Fe^0 to Fe^{3+} can be well distinguished from the broad anodic region of 1.3-2.2 V vs Li/Li^+. Although the as-prepared three Fe_2O_3-based electrodes present similar CV profiles, the discrepancies can still be observed. The Fe_2O_3@N/Cl-C-300 showed the largest cathodic current drop, which may be caused by the residue oxychloride according to the high chlorine content and also some unstable organics that were not carbonized. The Fe_2O_3@N/Cl-C-350 electrode demonstrated an evident improved reversibility. Moreover, it had a lower charge and discharge voltage gap than the Fe_2O_3@N/Cl-C-400 electrode due to that the small Fe_2O_3 nanoparticles were kept without agglomeration in the carbon matrix at a lower annealing temperature.

Fig. 5d-f show the discharge and charge profiles of the Fe_2O_3@N/Cl-C electrodes at 0.1A g^{-1} in the 1st, 2nd, 5th, and 10th cycles. The specific capacity was calculated on the basis of the total weight of the as-prepared Fe_2O_3@N/Cl-C material in the electrode. The Fe_2O_3@N/Cl-C-300, Fe_2O_3@N/Cl-C-350, and Fe_2O_3@N/Cl-C-400 electrodes deliver discharge capacities of 1246.1, 1363.6 and 1271.5 mAh g^{-1} at the first cycle, respectively. The corresponding Coulombic efficiencies are 62.3%, 74.1% and 65.0%, respectively. The Fe_2O_3@N/Cl-C-350 electrode possesses the best reversibility at the first cycle. This is consistent with the CV result. In the following

cycles, the median voltages of the discharge and charge curves are very close to the voltages of cathodic and anodic peaks in the CV patterns, respectively. The evident voltage plateaus were observed during discharge, as reflected by the distinct cathodic peaks in the CV patterns. The high reversible capacity is kept for the Fe_2O_3@N/Cl-C-350 electrode. For instance, the Fe_2O_3@N/Cl-C-350 electrode has a reversible discharge capacity of about 980 mAh g^{-1} at the 10th cycle. This capacity is much higher than 621 and 755 mAh g^{-1} of the Fe_2O_3@N/Cl-C-300 and Fe_2O_3@N/Cl-C-400 electrodes, respectively. The higher capacity of the Fe_2O_3@N/Cl-C-350 electrode may be ascribed to the efficient use of smaller and well distributed Fe_2O_3 nanoparticles in the carbon nanodisk with more active lithium storage sites such as N-5 and C-Cl species. The low reversible capacity of the Fe_2O_3@N/Cl-C-300 electrode may be caused by the aforementioned insufficient carbonization of PANI and decomposition of FeOCl, although the Fe_2O_3@N/Cl-C-300 material has a uniform morphology of nanodisk embedded with fine nanoparticles (Fig. 2g). The aggregation of Fe_2O_3 particles (Fig. 2i) at a higher annealing temperature of 400 ^oC led to a reduced reversible capacity of the Fe_2O_3@N/Cl-C-400 electrode. The result of rate performance (Fig. 5g) showed that the Fe_2O_3@N/Cl-C-300 electrode also exhibited depressed rate capability with very low discharge capacities of 256 mAh g^{-1} at 1 A g^{-1} and 60 mAh g^{-1} at 2 A g^{-1}. In contrast, the Fe_2O_3@N/Cl-C-350 electrode achieved high discharge capacities of 764 and 576 mAh g^{-1} at the same current densities, which are 73.1% and 56.4% of the reversible capacity at 0.1 A g^{-1} in the second cycle. These values are also high than

459 (54.7%) and 343 mAh g^{-1} (40.8%) of the Fe_2O_3@N/Cl-C-400 electrode. When the current rate was switched to 0.1 A g^{-1}, high discharge capacities of 1060.4 and 840 mAh g^{-1} was recovered for the Fe_2O_3@N/Cl-C-300 and Fe_2O_3@N/Cl-C-400 electrodes, respectively, indicating their admirable rate capability upon large current rate change.

The long-term cycling (Fig. 5h) at the low current rate of 0.1 A g^{-1} was carried out to investigate the cycling stability of the Fe_2O_3@N/Cl-C electrodes. The Fe_2O_3@N/Cl-C-300 electrode suffered from a large capacity decay upon cycling, and only 359.9 mAh g^{-1} was produced after 180 cycles. This capacity decay may be related to the dissolution of residue chloride species in the Fe_2O_3@N/Cl-C-300 material. Both the Fe_2O_3@N/Cl-C-350 and Fe_2O_3@N/Cl-C-400 electrodes exhibited good cycling stability with a high Coulombic efficiency of about 99% and discharge capacities of 955 and 762 mAh g^{-1}, respectively, after 180 cycles. The prolonged cycling further demonstrated the good cycling stability of the Fe_2O_3@N/Cl-C-350 electrode, which maintained a high stable discharge capacity of 995 mAh g^{-1} after 500 cycles at 0.5 A g^{-1} (Fig. S7). This performance is superior or comparable to those of some typical previously reported Fe_2O_3-based materials (Table S3) such as Cu-doped Fe_2O_3 (841 mAh g^{-1}/80 cycles) [57], Fe_2O_3@$NiMoO_4$-S (1001 mAh g^{-1}/100 cycles) [58], 3D netlike FeO_x/C (851.3 mAh g^{-1}/50 cycles) [59], yolk-shell Fe_2O_3@C (1013 mAh g^{-1}/80 cycles) [17], MWCNT/γ-Fe_2O_3 (723 mAh g^{-1}/310 cycles) [56], hierarchical hollow TiO_2 @Fe_2O_3 (530 mAh g^{-1}/200 cycles)[60], and Fe_2O_3-carbon nanofibers (820 mAh g^{-1}/100 cycles)[61]. Moreover, their preparation approaches such as a long time

hydrothermal synthesis with high pressure, special template or matrix, and high-temperature treatment are not required for our case, in which a new efficient, facile, and potentially scalable preparation strategy is developed. The FE-SEM and TEM images of the Fe_2O_3@N/Cl-C-350 material after a long cycling at 0.1 A g^{-1} showed that the agglomeration of the Fe_2O_3 nanoparticles was not observed (**Fig. 6**); instead, the particle size of Fe_2O_3 in the carbon nanodisk was refined by the repeated conversion reactions. Importantly, the pristine morphology of the nanodisk embedded with Fe_2O_3 nanoparticles was maintained, indicating the robust nanocomposite structure of the as-prepared Fe_2O_3@N/Cl-C-350 material and thus the superior cycling stability.

4. Conclusions

In summary, we have designed unique α-Fe_2O_3@cabon nanocomposites composed of N/Cl-doped carbon nanodisk and hematite nanoparticles via a new approach that annealed the precursor of laminated FeOCl@PANI heterostructure at a mild condition. This precursor was prepared by an efficient microwave synthesis of FeOCl and a subsequent facile polyaniline intercalation. The hematite nanoparticles were uniformly embedded in the dual-doped amorphous carbon nanodisk matrix with good contact through both physical and chemical interactions. The as-prepared composite structure can provide abundant active sites for effective ion storage and afford the volume variation during cycling. Consequently, the as-prepared Fe_2O_3@N/Cl-C-350 electrode achieved a high reversible capacity above 1000 mAh g^{-1} and maintained 955 mAh g^{-1} after a long cycling of 180 cycles at 0.1 Ah g^{-1}, indicating its superior

lithium-ion storage ability and cycling stability. This high reversible capacity can also be recovered after a rigorous current rate change in the range of 0.1~2 Ah g^{-1}, suggesting the decent rate performance. Our proposed material design as well as the facile, efficient, and potentially scalable synthesis strategy thereof are expected to produce high-performance iron oxide-based anode materials for various electrochemical energy storage systems. They may also be extended to other applications such as catalysis and chemical adsorption.

Acknowledgements

The support from the National Natural Science Foundation of China (grant no. 51674147), QingLan Project of Jiangsu Province, the Natural Science Foundation of the Jiangsu Higher Education Institutions (grant no. 16KJA430001), and the Priority Academic Program Development of Jiangsu Higher Education Institutions (PAPD) is acknowledged.

References

[1] Y. Liu, F.X. Lu, Y. Tang, M.Y. Liu, F.F. Tao, Y. Zhang, Effects of initial crystal structure of Fe_2O_3 and Mn promoter on effective active phase for syngas to light olefins, Appl. Catal. B 261 (2020) 118219.

[2] X.Y. Yang, X.Y. Zhang, Y.F. Ma, Y. Huang, Y.S. Wang, Y.S. Chen, Superparamagnetic graphene oxide–Fe_3O_4 nanoparticles hybrid for controlled targeted drug carriers, J. Mater. Chem. 19 (2009) 2710–2714.

[3] A. Kumar, M. Khan, L.P. Fang, I.M.C. Lo, Visible-light-driven N-TiO_2@SiO_2@Fe_3O_4 magnetic nanophotocatalysts: Synthesis, characterization, and photocatalytic degradation of PPCPs, J. Hazard. Mater. 370 (2019) 108–116.

[4] H.W. Fu, Q.Q. Wang, J.J. Ding, Y. Zhu, M. Zhang, C. Yang, S. Wang, Fe_2O_3 nanotube coating micro-fiber interferometer for ammonia detection, Sens. Actuat. B 303 (2020) 127186.

[5] F. Li, G.E. Luo, W.Y. Chen, Y.C. Chen, Y.P. Fang, M.T. Zheng, X.Y. Yu, Rational design and controllable synthesis of multishelled Fe_2O_3@SnO_2@C nanotubes as advanced anode material for lithium-/sodium-ion batteries, ACS Appl. Mater. Interfaces 11 (2019) 36949−36959.

[6] J. Zhan, K. Wu, X. Yu, M.J. Yang, X. Cao, B. Lei, D.Y. Pan, H. Jiang, M.H. Wu, α-Fe_2O_3 Nanoparticles decorated C@MoS_2 nanosheet arrays with expanded spacing of (002) plane for ultrafast and high Li/Na-ion storage, Small 15 (2019) 1901083.

[7] J.Y. Ma, X.T. Guo, Y. Yan, H.G. Xue, H. Pang, FeO_x-based materials for electrochemical energy storage, Adv. Sci. 5 (2018) 1700986.

[8] S.H. Yu, S. H. Lee, D. J. Lee, Y.E. Sung, T. Hyeon, Conversion Reaction-based oxide nanomaterials for lithium ion battery anodes, Small 12 (2016) 2146–2172.

[9] J. Wu, Y. Cao, H. Zhao, J. Mao, Z.P. Guo. The critical role of carbon in marrying silicon and graphite anodes for high-energy lithium-ion batteries. Carbon Energy 1 (2019) 57–76.

[10] B. Joshi, J.G. Lee, E. Samuel, H.S. Jo, T.G. Kim, M.T. Swihart, W.Y. Yoon, S.S. Yoon, Supersonically blown reduced graphene oxide loaded Fee Fe_3C nanofibers for lithium ion battery anodes, J. Alloys Compd. 726 (2017) 114-120.

[11] N. Song, F.Q. Ma, Y. Zhu, S.H. Chen, C. Wang, X.F. Lu, Fe_3C/nitrogen-doped carbon nanofibers as highly efficient biocatalyst with oxidase-mimicking activity for colorimetric sensing, ACS Sustainable Chem. Eng. 6 (2018) 16766−16776.

[12] W.M. Shen, W. Kou, Y. Liu, Y. Dai, W.J. Zheng, G.H. He, S.T.Wang, Y. Zhang, X.M. Wu, S. Fan, X.C. Li, Fe_3C-doped asymmetric porous carbon membrane binder-free integrated materials as high performance anodes of lithium-ion batteries, Chem. Eng. J. 368 (2019) 310–320.

[13] S. Sun, T. Zhai, C.L. Liang, S.V. Savilovc, H. Xia, Boosted crystalline/amorphous Fe_2O_3-δ core/shell heterostructure for flexible solid-state pseudocapacitors in large scale, Nano Energy 45 (2018) 390–397391.

[14] Y. Cao, Y.X. Yang, Z.H. Ren, N. Jian, M.X. Gao, Y.J. Wu, M. Zhu, F. Pan, Y.F Liu, H.G. Pan, A New Strategy to Effectively Suppress the initial capacity fading of iron oxides by reacting with $LiBH_4$, Adv. Funct. Mater. 27 (2017) 1700342.

[15] K.N. Zhao, M.Y. Wen, Y.F. Dong, L. Zhang, M.Y. Yan, W.W. Xu, C.J. Niu, L.

Zhou, Q.L. Wei, W.H. Ren, X.P. Wang, L.Q. Mai, Thermal induced strain relaxation of 1D iron oxide for solid electrolyte interphase control and lithium storage improvement, Adv. Energy Mater. 7 (2017) 1601582.

[16] S.H. Luo, D.B. Hu, H. Liu, J.Z. Li, T.F. Yi, Hydrothermal synthesis and characterization of α-Fe_2O_3/C using acid-pickled iron oxide red for Li-ion batteries, J. Hazard. Mater. 5 (2019) 714-721.

[17] Z.M. Zheng, Y. Zao, Q.B. Zhang, Y. Cheng, H.X. Chen, K.L. Zhang, M.S.Wang, D.L. Peng, Robust erythrocyte-like Fe_2O_3@carbon with yolk-shell structures as high performance anode for lithium ion batteries, Chem. Eng. J. 347 (2018) 563–573.

[18] T.C. Jiang, F.X. Bu, X.X. Feng, I. Shakir, G.L. Hao, Y.X. Xu, Porous Fe_2O_3 Nanoframeworks Encapsulated within three-dimensional graphene as high-performance flexible anode for lithium-ion battery, ACS Nano 11 (2017) 5140−5147.

[19] J.F. Ni, M.L. Sun, L. Li, Highly efficient sodium storage in iron oxide nanotube arrays enabled by built-in electric field, Adv. Mater. 31 (2019) 1902603.

[20] M.L. Sun, Z.Z. Wang, J.F. Ni, L. Li, Dual-doped hematite nanorod arrays on carbon cloth as a robust and flexible sodium anode, Adv. Funct. Mater. 30 (2020) 1910043.

[21] J.S. Cho, Y.J. Hong, Y.C. Kang, Design and synthesis of bubble-nanorod-structured Fe_2O_3–carbon nanofibers as advanced anode material for Li-ion batteries, ACS Nano 9 (4) 4026–4035.

[22] Z.M. Zheng, P. Li, J.S. Huang, H.D. Liu, Y. Zao, Z.L. Hu, L. Zhang, H.X. Chen,

M.S.Wang, D.L.Peng, Q.B. Zhang, High performance columnar-like Fe_2O_3@carbon composite anode via yolk@shell structural design, J. Energy Chem. 41 (2020) 126–134.

[23] X.Y. Zhao, Z.R. Zhao-Karger, D. Wang, M. Fichtner, Metal oxychlorides as cathode materials for chloride ion batteries, Angew. Chem. Int. Ed. 52 (2013) 13621 – 13624.

[24] T.T. Yu, Q. Li, X.Y. Zhao, H. Xia, L.Q. Ma, J.L. Wang, Y.S. Meng, X.D. Shen, Nanoconfined iron oxychloride material as a high-performance cathode for rechargeable chloride ion batteries, ACS Energy Lett. 2 (2017) 2341−2348.

[25] C.G. Wu, D.C.D. Groot, H.O. Marcy, J. L. Schindler, C.R. Kannewurf, T. Bakas, V. Papaefthymiou, W. Hirpo, J.P. Yesinowski, Y.-J. Liu, M.G. Kanatzidis, Reaction of aniline with FeOCl. Formation and ordering of conducting polyaniline in a crystalline layered host, J. Am. Chem. Soc. 117 (1995) 9229-9242.

[26] Y. Matsuo, S. Higashika, K. Kimura, Y. Miyamoto, T. Fukutsuka, Y. Sugie, Synthesis of polyaniline-intercalated layered materials via exchange reaction, J. Mater. Chem. 12 (2002) 1592–1596.

[27] S.F. Scully, R. Bissessur, D.C. Dahn, G. Xie, In situ polymerization/intercalation of substituted anilines into iron (III) oxychloride, Solid State Ion 181 (2010) 933–938.

[28] T.T. Yu, R.J. Yang, X.Y. Zhao, X.D. Shen, Polyaniline-intercalated FeOCl cathode material for chloride-ion batteries, ChemElectroChem 6 (2019) 1–8.

[29] H.S.O. Chan, M.Y. B. Teo, E. Khor, C.N. Lim, Thermal analysis of conducting polymers part .I. Thermogravimetry of acid-doped polyanilines, J. Therm. Anal. 35

(1989) 765-774.

[30] Y.D. Dai, Z.i Yu, H.B. Huang, Y. He, T. Shao, Y.F. Hsia, Thermal decomposition of iron oxychloride as studied by thermal analysis, X-ray diffraction and Mössbauer spectroscopy, Mater. Chem. Phys. 79 (2003) 94–97.

[31] Z. Rozlivkova, M. Trchova, M. Exnerova, J. Stejskal, The carbonization of granular polyaniline to produce nitrogen-containing carbon, Synth. Met. 161 (2011) 1122–1129.

[32] F. Cheng, K.L. Huang, S.Q. Liu, J.L. Liu, R.J. Deng, Surfactant carbonization to synthesize pseudocubic α-Fe_2O_3/C nanocomposite and its electrochemical performance in lithium-ion batteries, Electrochim. Acta 56 (2011) 5593–5598.

[33] M. Trchova, I. Syedenkova, E. N. Konyushenko, J. Stejskal, P. Holler, G. C iric-Marjanovic, Evolution of Polyaniline Nanotubes: The oxidation of aniline in water, J. Phys. Chem. B 110 (2006) 9461-9468.

[34] Z. Moravkova, M. Trchova, M. Exnerova, J. Stejskal, The carbonization of thin polyaniline films, Thin Solid Films 520 (2012) 6088–6094.

[35] P. Bober, J. Kovarova, J. Pfleger, J. Stejskal, M. Trchova, I. Novak, D. Berek, Twin carbons: The carbonization of cellulose or carbonized cellulose coated with a conducting polymer, polyaniline, Carbon 109 (2016) 836e842.

[36] K. Kakaei, M. Hamidi, S. Husseindoost, Chlorine-doped reduced graphene oxide nanosheets as an efficient and stable electrode for supercapacitor in acidic medium, J. Colloid Interface Sci. 479 (2016) 121–126.

[37] X.J. Yang, P.F. Tian, X.M. Zhang, X. Yu, T. Wu, J. Xu, Y.F. Han, The generation

of hydroxyl radicals by hydrogen peroxide decomposition on FeOCl/SBA-15 catalysts for phenol degradation, AICE J 61 (2015) 166-176.

[38] C.C. Wan, Y. Jiao, W.H. Bao, H. Gao, Y.Q. Wu, J. Li, Self-stacked multilayer FeOCl supported on a cellulose-derived carbon aerogel: a new and high-performance anode material for Supercapacitors, J. Mater. Chem. A 7 (2019) 9556-9564.

[39] H.J. Wu, G.L. Wu, L.D. Wang, Peculiar porous α-Fe_2O_3, γ-Fe_2O_3 and Fe_3O_4 nanospheres: Facile synthesis and electromagnetic properties, Powder Technol. 269 (2015) 443–451.

[40] H. Liu, S.H. Luo, D.B. Hu, X. Liu, Q. Wang, Z.Y. Wang, Y.L. Wang, L.J. Chang, Y.G. Liu, T.F. Yi, Y.H. Zhang, A.M. Hao, Design and synthesis of carbon-coated α-Fe_2O_3@Fe_3O_4 heterostructured as anode materials for lithium ion batteries, Appl. Surf. Sci. 495 (2019) 143590.

[41] R.O. Dillon, J.A. Woollam, Use of Raman scattering to investigate disorder and crystallite formation in as-deposited and anriealed carbon films, Phys. Rev. B 29 (1984) 3482-3489.

[42] X.R. Zeng, T.M. Ko, Structure–conductivity relationships of iodine-doped polyaniline, J. Poly. Sci. Poly. Phys. 35 (1997) 1993-2001.

[43] S. Golczak, A. Kanciurzewsk, M. Fahlman, K.Langer, J.J. Langer, Comparative XPS surface study of polyaniline thin films, Solid State Ion. 179 (2008) 2234–2239.

[44] T.T. Zhu, J. Zhou, Z.H. Li, S.J. Li, W.J. Si, S.P. Zhuo, Hierarchical porous and N-doped carbon nanotubes derived from polyaniline for electrode materials in supercapacitors, J. Mater. Chem. A 2 (2014) 12545-12551.

[45] A.F. Perez-Cadenas, F. J. Maldonado-Hodar, C. Moreno-Castilla, On the nature of surface acid sites of chlorinated activated carbons, Carbon 41 (2003) 473–478.

[46] W. Chang, J. Qu, S.M. Hao, Y.J. Zhang, Z.-G. Jiang, Z.Z. Yu, Effects of graphene quality on lithium storage performances of Fe_3O_4/thermally reduced graphene oxide hybrid anodes, ChemElectroChem 6 (2019) 1–9.

[47] S. Golcza, A. Kanciurzewsk, M. Fahlman, K. Langer, J.J. Langer, Comparative XPS surface study of polyaniline thin films, Solid State Ion. 179 (2008) 2234–2239.

[48] G.C. Jia, H.W. Wang, D.L. Chao, H.Y. He, N.H. Tiep, Y.Q. Zhang, Z. Zhang, H. J. Fan, Ultrathin $MoSe_2$@N-doped carbon composite nanospheres for stable Na-ion storage, Nanotechnology 28 (2017) 42LT01.

[49] M. Vujkovic, N. Gavrilov, I. Pasti, J. Krstic, J. Travas-Sejdic, G. Ciric-Marjanovic, S,Mentus, Superior capacitive and electrocatalytic properties of carbonized nanostructured polyaniline upon a low-temperature hydrothermal treatment, Carbon 64 (2013) 472 –486.

[50] S. Wang, A.A. Rogachev, M.A. Yarmolenko, A.V. Rogachev, X.H.Jiang , M.S. Gaur, P.A. Luchnikov, O.V. Galtseva, S.A. Chizhikf, Structure and properties of polyaniline nanocomposite coatings containing gold nanoparticles formed by low-energy electron beam deposition, Appl. Surf. Sci. 428 (2018) 1070–1078.

[51] Y.G. Xu, Y. Ma, X.Y. Ji, S.Q. Huang, J.X. Xia, M. Xie, J.Yan, H. Xu, H.M. Li, Conjugated conducting polymers PANI decorated $Bi_{12}O_{17}Cl_2$ photocatalyst with extended light response range and enhanced photoactivity, Appl. Surf. Sci. 464 (2019) 552–561.

[52] C. Chen, T.T. Yu, M. Yang, X.Y. Zhao, X.D. Shen, An all-solid-state rechargeable chloride ion battery, Adv. Sci. (2019) 1802130.

[53] S.H. Shen, X.H. Xia, Y. Zhong, S.J. Deng, D. Xie, B. Liu, Y. Zhang, G.X. Pan, X.L. Wang, J.P. Tu, Implanting niobium carbide into trichoderma spore carbon: a new advanced host for sulfur cathodes, Adv. Mater. 31(2019) 1900009.

[54] J.T. Xu, I.Y. Jeon, J.M. Seo, S.X. Dou , L.M. Dai, J.B. Baek, Edge-selectively halogenated graphene nanoplatelets (XGnPs, X = Cl, Br, or I) prepared by ball-milling and used as anode materials for lithium-ion batteries, Adv. Mater. 26 (2014) 7317–7323.

[55] M.J. Park, I.Y. Jeon, J. Ryu, H. Jang, J.B. Back, J. Cho, Edge-halogenated graphene nanoplatelets with F, Cl, or Br as electrocatalysts for all-vanadium redox flow batteries, Nano Energy 26 (2016) 233–240.

[56] P. Bhattacharya, M. Kota, D. H. Suh, K. C. Roh, H. S. Park, Biomimetic spider-web-Like composites for enhanced rate capability and cycle life of lithium ion battery anodes, Adv. Energy Mater. (2017) 1700331.

[57] J.L. Zhang, V.W.H. Lau, C.Z. Liao, K.W. Wong, G.H. Lee, F. Zou, C.K. Chang, H.S. Sheu, Y.M. Kang, Controlling the valence state of Cu dopant in α-Fe_2O_3 anodes: effects on crystal structure and the conversion reactions with alkali ions, Chem. Mater. 29 (2019) 1268-1279.

[58] H.L. Yue, G.M. Wang, R.C. Jin, Q.Y. Wang, Y.M. Cui, S.M. Gao, Sulfur-doped amorphous $NiMoO_4$ on crystalline Fe_2O_3 nanorods for enhanced lithium storage Performance, J. Mater. Chem. A. 6 (2018) 23819–23827.

[59] M. Li, H.R. Du, L. Kuai, K.F. Huang, Y.Y. Xia, B.Y. Geng, Scalable dry production process of a superior 3D net-like carbon-based iron oxide anode material for lithium-ion batteries, Angew. Chem. Int. Ed. 56 (2017) 12649–12653.

[60] J.S. Luo, X.H. Xia, Y.S. Luo, C. Guan, J.L. Liu, X.Y. Qi ,C.F. Ng, T. Yu, H. Zhang, H.J. Fan, Rationally designed hierarchical TiO_2@Fe_2O_3 hollow nanostructures for improved lithium ion storage, Adv. Energy Mater. 3 (2013) 737–743.

[61] X. Zhang, H.H. Liu, S. Petnikota, S. Ramakrishna, H.J. Fan, Electrospun Fe_2O_3–carbon composite nanofibers as durable anode materials for lithium ion batteries, J. Mater. Chem. A, 2 (2014) 10835–10841.

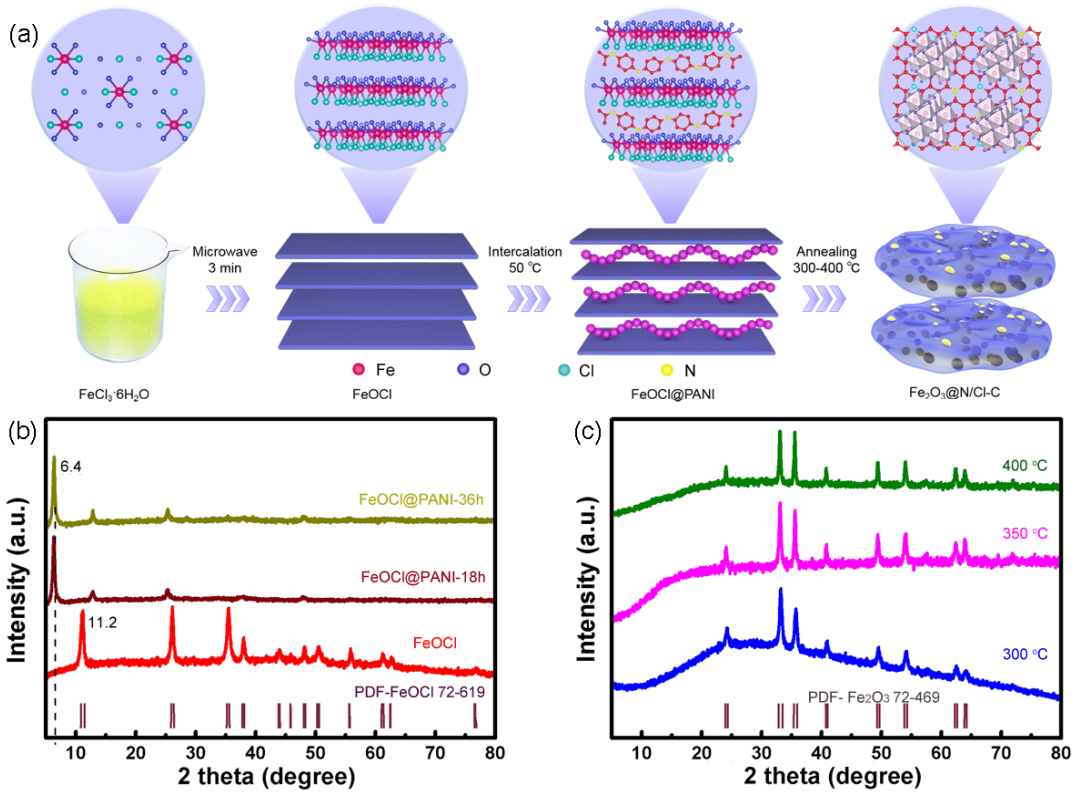

Fig. 1. (a) Schematic fabrication process of the Fe_2O_3@N/Cl-C material. XRD patterns of (b) the as-prepared FeOCl, laminated FeOCl@PANI, and (c) Fe_2O_3@N/Cl-C materials.

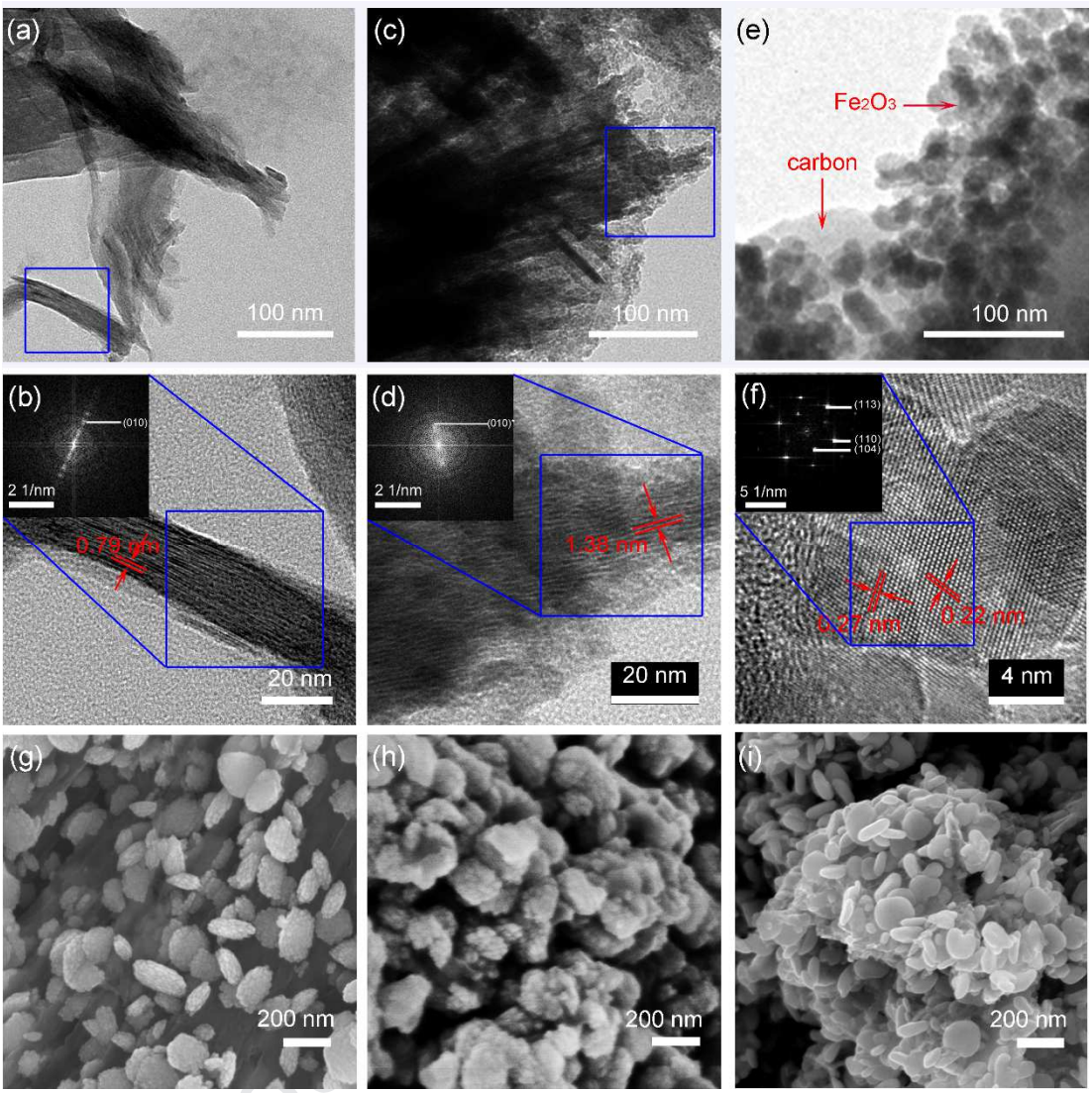

Fig. 2. TEM, HRTEM, and the corresponding FFT patterns of (a, b) the as-prepared FeOCl, (c, d) laminated FeOCl@PANI, (e, f) Fe_2O_3@N/Cl-C-350. SEM images of the Fe_2O_3@N/Cl-C materials prepared at (g) 300, (h) 350, and (i) 400 °C.

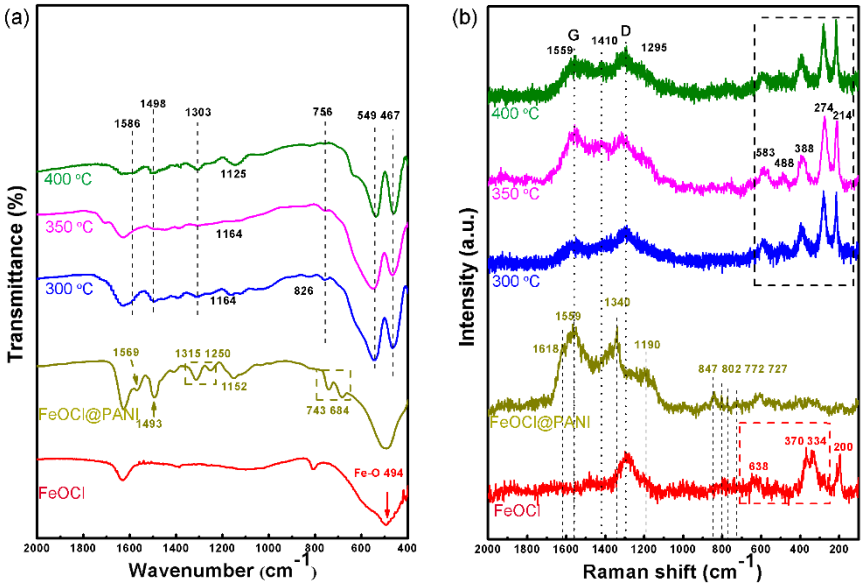

Fig. 3. (a) FTIR spectra and (b) Raman spectra of the as-prepared FeOCl, laminated FeOCl@PANI, and Fe_2O_3@N/Cl-C materials.

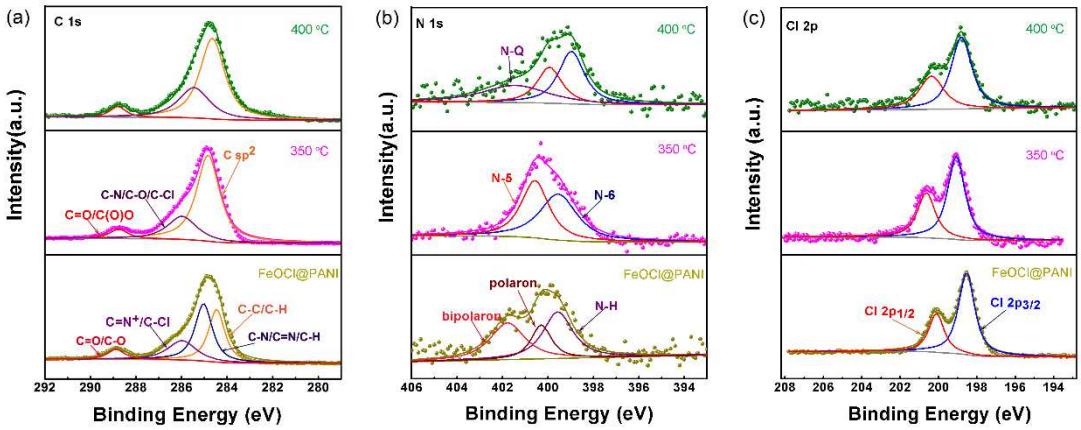

Fig. 4. XPS spectra of the as-prepared laminated FeOCl@PANI and Fe_2O_3@N/Cl-C materials: (a) C 1s, (b) N 1s, and (c) Cl 2p.

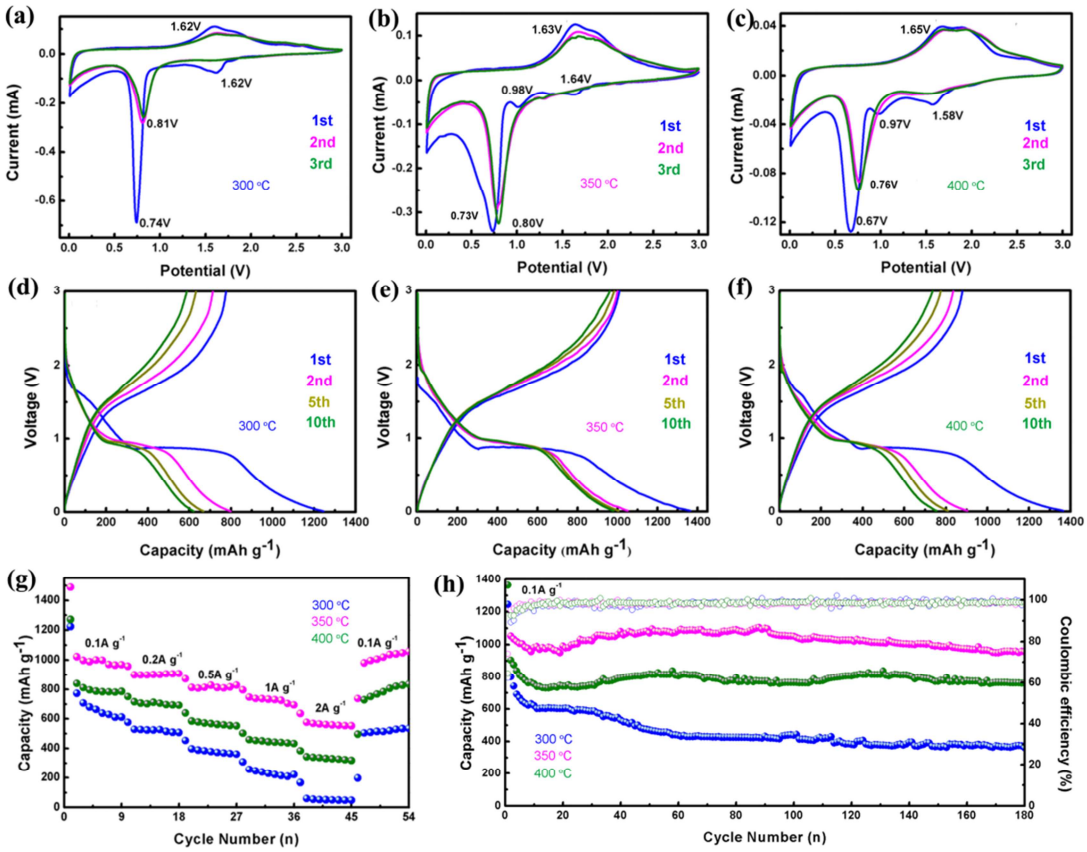

Fig. 5. (a-c) CV curves (0.05 mV s^{-1}), (d-f) discharge and charge curves (0.1 A g^{-1}), (g) rate performance, and (h) cycling performance of the Fe_2O_3@N/Cl-C-300, Fe_2O_3@N/Cl-C-350, and Fe_2O_3@N/Cl-C-400 electrodes.

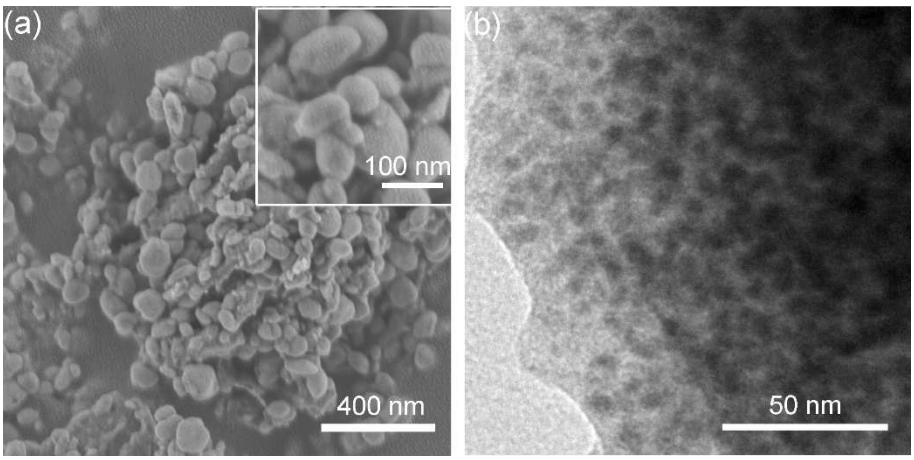

Fig. 6. (a) SEM and (b) TEM images of the Fe_2O_3@N/Cl-C-350 electrode after 120 cycles.

- Developing a novel, facile and scalable synthesis approach for hematite/carbon nanocomposites
- N/Cl-doped carbon nanodisk-encapsulated hematite anode shows robust structure for Li-ion storage
- High reversible capacity, decent rate capability and superior cycling performance are achieved

Declaration of interests

☒ The authors declare that they have no known competing financial interests or personal relationships that could have appeared to influence the work reported in this paper.

☐The authors declare the following financial interests/personal relationships which may be considered as potential competing interests: